Journal of MATERIALS RESEARCH

Invited Feature Paper
DOI:10.1557/s43578-022-00784-y

EARLY CAREER SCHOLARS IN MATERIALS SCIENCE 2023

ANNUAL ISSUE

Nucleation and growth behavior of multicomponent secondary phases in entropy-stabilized oxides

Alexander D. Dupuy[1,a], Mohammed Reda Chellali[2], Horst Hahn[1,2,3], Julie M. Schoenung[1]

[1] Department of Materials Science and Engineering, University of California, Irvine, USA
[2] Institute of Nanotechnology, Karlsruhe Institute of Technology, 76344 Eggenstein-Leopoldshafen, Germany
[3] KIT-TUD Joint Research Laboratory Nanomaterials, Institute of Materials Science, Technical University Darmstadt, 64206 Darmstadt, Germany
[a] Address all correspondence to this author. e-mail: dupuya@uci.edu

Received: 27 July 2022; accepted: 3 October 2022

The rocksalt structured (Co,Cu,Mg,Ni,Zn)O entropy-stabilized oxide (ESO) exhibits a reversible phase transformation that leads to the formation of Cu-rich tenorite and Co-rich spinel secondary phases. Using atom probe tomography, kinetic analysis, and thermodynamic modeling, we uncover the nucleation and growth mechanisms governing the formation of these two secondary phases. We find that these phases do not nucleate directly, but rather they first form Cu-rich and Co-rich precursor phases, which nucleate in regions rich in Cu and cation vacancies, respectively. These precursor phases then grow through cation diffusion and exhibit a rocksalt-like crystal structure. The Cu-rich precursor phase subsequently transforms into the Cu-rich tenorite phase through a structural distortion-based transformation, while the Co-rich precursor phase transforms into the Co-rich spinel phase through a defect-mediated transformation. Further growth of the secondary phases is controlled by cation diffusion within the primary rocksalt phase, whose diffusion behavior resembles other common rocksalt oxides.

Alexander Dupuy

Dr. Alexander Dupuy is a project scientist in the Department of Materials Science and Engineering at the University of California, Irvine, where he studies the processing, properties, and phase transformation behavior of entropy stabilized oxides. He received his B.S in Mechanical Engineering from the University of California Riverside (UCR) in 2009. His undergraduate research involved investigating gradient induced inhomogeneity found in the Spark Plasma Sintering (SPS) process. In 2011 he went on to receive his M.S in Mechanical Engineering from UCR where he studied pressure induced densification mechanisms in nanomaterials processed using SPS. In 2016 he received his Ph.D. in Mechanical Engineering from UCR. His doctoral work focused on the processing and measurement of optical and ferroelectric ceramics. Much of Dr. Dupuy's research has involved processing of functional and structural inorganic materials (ceramics, alloys, intermetallics, composites) with novel or customized phase and microstructural conditions, particularly involving nanostructuring and metastable states. He is particularly interested in the intersection between processing, microstructure, and phase transformations, and their influence on a wide range of material behaviors, including; optical, ferroelectric, ferromagnetic, multiferroic, electrical, mechanical, and thermal properties. He also has a strong interest in materials with the potential for interesting phase transformation behavior, such as entropy stabilized oxides (entropic phase transformation) and ferroelectric materials (morphotropic/polymorphic phase boundaries), and how these transformations can be leveraged to enhance properties.

Introduction

Since their discovery in 2015 [1], high-entropy oxides (HEOs) have garnered significant attention due to their wide composition space and interesting behavior [2]. A HEO contains five or more oxide components that are mixed in equimolar amounts and form a single-phase solid-solution structure after processing. HEO materials show promise in a range of applications, such as electronics [3], batteries [4], and catalysts [5]. Despite their compositional complexity, HEOs can be successfully fabricated in forms other than bulk ceramics, including nanopowders [6] and thin films [7]. Additionally, the concepts behind high-entropy design has been applied to non-oxide systems as well, including silicides [8], borides [9], and carbides [10].

While the incorporation of five or more oxides will result in a material with high entropy, this does not guarantee that the respective HEO will be truly *entropy-stabilized*. An entropy-stabilized oxide (ESO) must have a metastable entropy-driven single-phase state that overcomes the free energy of an equilibrium enthalpy-driven multi-phase state. The metastability of the entropy-driven state arises from the fact that the contribution of entropy to the Gibb's free energy is regulated by temperature. The temperature sensitivity of entropy leads to a competition between the entropy-driven phase state and the enthalpy-driven phase state, resulting in a *reversible* entropic phase transformation.

In our previous work, we demonstrated that this reversible phase transformation in the transition metal oxide (Co,Cu,Mg,Ni,Zn)O (referred to here as TM-ESO) gave rise to a continuum of phase heterogeneity that could be modified by heat treating within a specific temperature window (650–850 °C) [11]. For TM-ESO, the entropy-driven state consists of a single-phase rocksalt solid-solution crystal structure, which is stable at temperatures above the entropic transformation temperature (~ 850 °C). The phase heterogeneity manifests as the formation of Cu-rich tenorite and Co-rich spinel phases [12]. The enthalpy-driven multi-phase state, therefore, consists of the primary rocksalt phase along with the Cu-rich tenorite and the Co-rich spinel secondary phases, with the at.% of the phases being controllable through heat treatment temperature and time. These secondary phases form as particles with needle- or sphere-like shapes, with the morphology being partly determined by the grain size after sintering [13]. We observe that the phase transformation provides unparalleled microstructural control, giving ESO materials an additional lever for tuning their structural and functional behavior.

Atom probe tomography (APT) has emerged as a powerful instrument for chemical analysis at the nanoscale, due to its sub-nanoscale resolution and elemental detection sensitivity [14]. APT instruments can analyze the chemical distribution of a selected nanoscale volume in 3D. APT has been successfully used to analyze a wide range of material systems, including high-entropy alloys [15, 16], which contain five or more metallic elements and were the primary inspiration behind HEOs. In our previous work, we analyzed *single-phase* TM-ESO particles and bulk samples using a combination of X-ray diffraction (XRD), scanning electron microscopy (SEM), and APT [17, 18]. We found that these single-phase TM-ESO samples were chemically homogeneous down to the nanoscale, despite being prepared using a variety of different chemical synthesis and sintering methods. Additionally, we demonstrated that the combination of XRD, SEM, and APT provides a powerful approach for studying the chemical distribution in these complex materials across a wide range of length scales.

In our other previous work, we focused on characterizing the *secondary phases* using microscopy [11] as well as identifying how the phase transformation influences the electronic structure of TM-ESO [12]. However, the nucleation and growth mechanisms governing the formation of the secondary phases are currently unknown. Understanding the mechanisms behind the secondary-phase formation in TM-ESO will allow for greater control over microstructure and behavior. In the current work, we study the nucleation and growth behavior of both the Cu-rich tenorite and Co-rich spinel secondary phases in TM-ESO. We have prepared samples with two different grain sizes and heat treated them to stimulate meaningful secondary-phase formation. We then used a combination of APT characterization, kinetic analysis, and thermodynamic modeling to construct a nucleation and growth sequence for the secondary phases. We find that the Cu-rich tenorite and Co-rich spinel secondary phases follow a complex multistep nucleation and growth process. Additionally, the phase transformation mechanisms are distinct between the two phases.

Results

Microstructure and phase state

XRD confirms that the as-sintered TM-ESO samples consolidated using conventional sintering display a single-phase rocksalt crystal structure with no signs of extraneous peaks [Fig. 1(a)]. SEM micrographs of fracture surfaces reveal that these bulk samples display large equiaxed grains with an average grain size of 15 μm [Fig. 1(b)]. We hereafter refer to this as the "coarse-grained" sample. These coarse-grained samples are consolidated using high temperatures (1100 °C) and long hold times (12 h), leading to the significant grain growth and equiaxed microstructure observed.

Bulk TM-ESO samples consolidated using spark plasma sintering (SPS) also display a primarily rocksalt

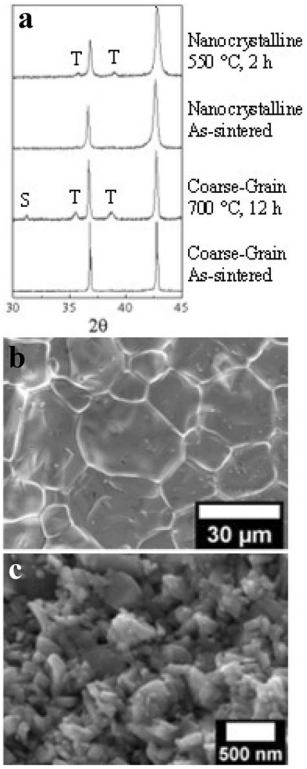

Figure 1: Phase state and microstructure of consolidated and heat-treated TM-ESO samples. (a) X-ray diffraction patterns for the coarse-grained and nanocrystalline TM-ESO samples before and after heat treatment. Peaks corresponding to the secondary phases are labeled as 'T' for the tenorite phase and 'S' for the spinel phase. (b) Fracture surface micrograph of an as-sintered coarse-grained sample. (c) Fracture surface micrograph of an as-sintered nanocrystalline sample.

crystal structure, as well as a minor amount of tenorite phase [Fig. 1(a)]. Some minor amount of secondary phase forms after consolidation due to the SPS processing being performed at 700 °C, which is within the phase transformation window for TM-ESO [11]. These samples display a nanocrystalline microstructure (average grain size of 90 nm) with non-equiaxed grains [Fig. 1(c)]. We hereafter refer to this as the "nanocrystalline" sample. The low consolidation temperature and short sintering time allow the single-phase state and nanocrystallinity to be retained from the TM-ESO nanopowders.

Heat treating the coarse-grained sample at 700 °C for 12 h yields an XRD pattern with three distinct sets of peaks, corresponding to the entropy-stabilized rocksalt phase, a Cu-rich tenorite secondary phase, and a Co-rich spinel secondary phase [12]. The Cu-rich tenorite phase and Co-rich spinel phase are labeled "T" and "S," respectively, in Fig. 1(a). Heat treating the nanocrystalline sample at 550 °C for 2 h results in the formation of secondary phases, yielding an XRD pattern with peaks corresponding to the rocksalt phase and the Cu-rich tenorite phase

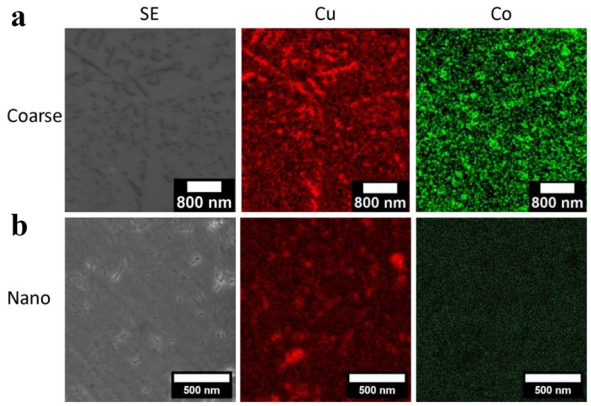

Figure 2: Investigation of the secondary phases at the micro-scale. Scanning electron micrograph and the corresponding Cu (red) and Co (green) EDS elemental maps for the heat-treated (a) coarse-grained and (b) nanocrystalline TM-ESO samples.

[Fig. 1(a)]. The Co-rich spinel phase is not observed in the XRD pattern for this sample.

SEM and energy-dispersive X-ray spectroscopy (EDS) were used to analyze the secondary phases at the microscopic length scale and to determine secondary-phase particle sizes. Cu-rich sphere-like and needle-like particles, corresponding to the Cu-rich tenorite phase, are observed in the coarse-grained samples [Fig. 2(a)]. These Cu-rich particles have Feret diameters ranging from 40 to 700 nm, with an average Feret diameter of 200 nm. Co-rich spinel particles are also observed and adopt a primarily sphere-like morphology with Feret diameters ranging from 40 to 440 nm and an average Feret diameter of 170 nm. The Cu-rich tenorite particles in the nanocrystalline sample do not form as spherical- or needle-like morphologies [Fig. 2(b)]. Instead they are similar in size and shape to the nanocrystalline grains, which is consistent with our previous observations that the tenorite particles encompass an entire grain in nanocrystalline TM-ESO samples [11]. These Cu-rich tenorite particles have Feret diameters ranging from 40 to 170 nm, with an average Feret diameter of 70 nm. Spinel particles are not observed in the EDS results for the nanocrystalline sample, which is consistent with our XRD results [Fig. 1(a)]. Hereafter, we refer to the Cu-rich tenorite secondary-phase particles and the Co-rich spinel secondary-phase particles observed through SEM simply as "tenorite particles" and "spinel particles," respectively.

Nanoscale chemical analysis

SEM/EDS can identify the distribution and morphology of the secondary phases across a range of length scales (40–700 nm), allowing for the equilibrium behavior of the secondary phases to be observed. To better understand the nucleation process, however, an even finer scale is needed. Thus, APT was used to

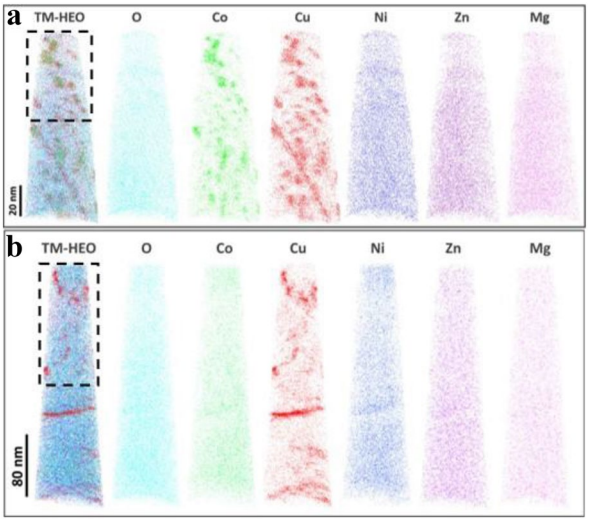

Figure 3: Investigation of the chemical distribution at the nanoscale. Atom probe tomograph (APT) 3D chemical distribution maps for the heat-treated (a) coarse-grained and (b) nanocrystalline TM-ESO samples. The dashed black boxes indicate the regions where isoconcentration surface analysis was performed.

observe the elemental distribution at length scales < 100 nm. A three-dimensional APT reconstruction of all six elements in the coarse-grained sample is observed in Fig. 3(a), with individual atoms being represented by color-coded dots. Regions of Cu (red) and Co (green) segregation are distributed throughout the volume, while the other four elements appear homogeneous. To distinguish these regions of enrichment from the tenorite and spinel particles observed in SEM, we refer to these regions observed using APT as Cu-rich and Co-rich "nanoparticles".

In order to highlight the features of the Cu-rich and Co-rich nanoparticles, isoconcentration surfaces were constructed from the region contained in the dashed black box in Fig. 3(a). The analyzed volume contains Cu-rich nanoparticles having both spherical and elongated morphologies [Fig. 4(a)]. Additionally, the analyzed volume contains a grouping of primarily spherical Co-rich nanoparticles. From the APT isoconcentration surfaces, it is possible to quantitatively assess the size of these nanoparticles. The Cu-rich nanoparticles have an average Feret diameter of 3.0 nm (radius of 1.5 nm), while the Co-rich nanoparticles have an average Feret diameter of 2.0 nm (radius of 1.0 nm).

Proxigrams were used to measure the concentration of the nanoparticles and the surrounding area [19]. A concentration proxigram of a representative Cu-rich nanoparticle in the coarse-grained sample is shown in Fig. 4(b). Three distinct regions of the concentration profile are observed: the primary TM-ESO phase, the Cu-rich nanoparticle, and the compositional transition region between the two phases. The boundary between the primary TM-ESO phase and the compositional transition region is arbitrarily defined on the x-axis as 0 (zero)

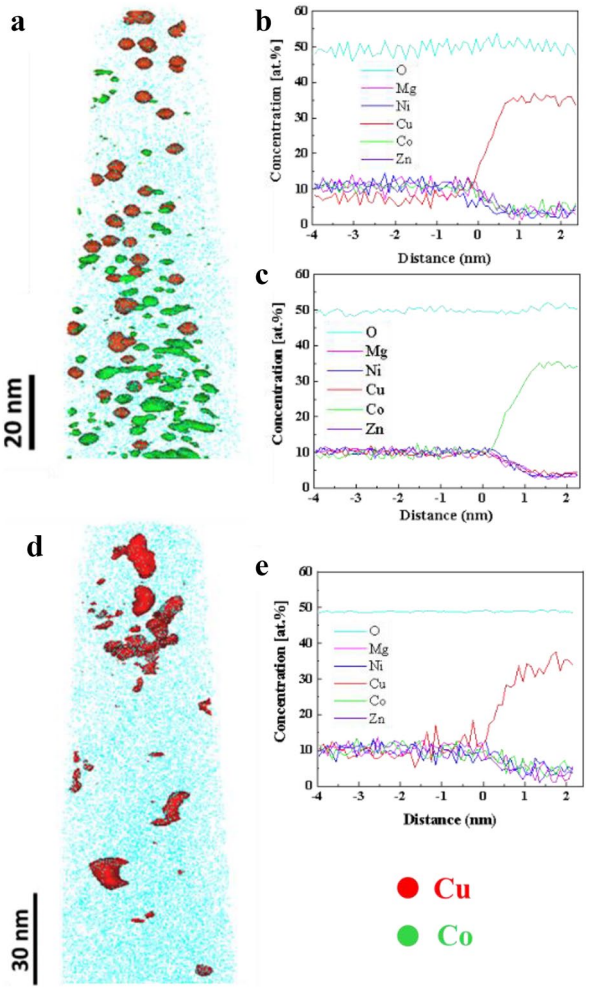

Figure 4: Interrogation into nanoparticle chemistry in TM-ESO samples. For coarse-grained TM-ESO: (a) APT 3D reconstruction showing isoconcentration surfaces of Cu (red) and Co (green). (b) A representative proxigram of a Cu-rich nanoparticle and the surrounding rocksalt primary phase. (c) A representative proxigram of a Co-rich nanoparticle. For nanocrystalline TM-ESO: (d) APT 3D reconstruction showing isoconcentration surfaces of Cu. (e) A representative proxigram of a Cu-rich nanoparticle and the surrounding rocksalt primary phase.

nm. The observed nanoparticle is enriched in Cu and depleted in the other cations relative to the primary rocksalt phase. A gradual change in the cation concentration is observed in the compositional transition region between the Cu-rich nanoparticle and the primary phase, while the oxygen concentration remains constant. The composition of the nanoparticle plateaus at a distance of > 1 nm indicates that the composition has reached equilibrium. The Cu-rich nanoparticles are not pure CuO, but instead have the form of $(Cu_xM_{x-1})O$, where M is the sum of the other cations (M = Co,Mg,Ni,Zn). The evaluated Cu-rich nanoparticles have an average Cu concentration of 37 at.%, an oxygen concentration of 50 at.%, and M = 13 at.%. A summary of the chemical composition of the Cu-rich nanoparticles is provided in Fig. 5(a).

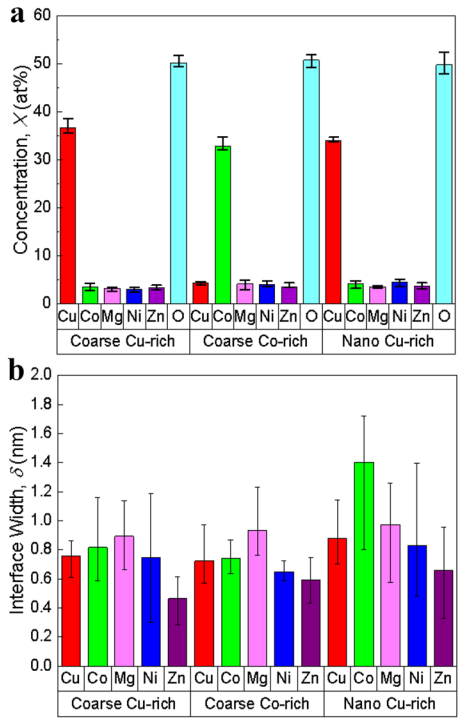

Figure 5: Composition and interface width for the TM-ESO precursor-phase nanoparticles. (a) Concentration, *X*, and (b) interface width, *δ*, values for the five cations in the Cu-rich and Co-rich precursor-phase nanoparticles determined for the coarse-grained and nanocrystalline TM-ESO samples using APT. Error bars correspond to the range of observed values.

A concentration proxigram of a representative Co-rich nanoparticle in the coarse-grained sample is provided in Fig. 4(c). Again, three distinct regions of the concentration profile are observed: the primary TM-ESO phase, the Co-rich nanoparticle, and the compositional transition region. The nanoparticle itself is enriched in Co and deficient in the other cations, having the approximate form of $(Co_xM_{x-1})O$ (M = Cu,Mg,Ni,Zn). A composition plateau is reached at a distance of > 1 nm, indicating that this is the equilibrium composition for the Co-rich phase. The evaluated Co-rich nanoparticles have an average Co concentration of 33 at.%, an average oxygen concentration of 51 at.%, and M = 16 at.% [Fig. 5(a)].

The diffusion of atoms during the early stages of secondary-phase nucleation will lead to the formation of a diffuse compositional interface region [20]. The thickness and form of these compositional interfaces can therefore provide insight into the nucleation and growth mechanisms of the Cu- and Co-rich nanoparticles. Diffuse concentration profiles, such as those acquired from APT, can be fit to a sigmoid function of the form [21]:

$$\frac{X - X_m}{X_p - X_m} = \frac{1}{1 + e^{-\eta(z - z_0)}}, \quad (1)$$

where X is the concentration at position z, X_m is the concentration of the TM-ESO rocksalt phase, X_p is the concentration of the secondary-phase nanoparticle, η is a fitting parameter related to the slope of the straight-line segment of the sigmoid, and z_0 is the center of the straight-line segment (the inflection point).

The compositional interface width (δ) between the secondary and primary phase can then be calculated from

$$\delta = \frac{\Delta X}{\left(\frac{dX}{dz}\right)_{z_0}} = \frac{4}{\eta}, \quad (2)$$

where ΔX is the difference in concentration between the secondary-phase nanoparticle and the primary phase and $\left(\frac{dX}{dz}\right)_{z_0}$ is the slope of the straight-line segment at position z_0.

Using Eqs. [1] and [2], values for δ, for both the Cu-rich and Co-rich nanoparticles in the coarse-grained sample, were calculated from the APT concentration profiles. The average and range of δ values for the cations are displayed in Fig. 5(b). Note that δ for oxygen is not defined because it remains constant throughout the transition between the primary phase and tenorite phase. For the Cu-rich nanoparticles, the values of δ for Cu fall in the range 0.6–0.9 nm, with an average value of 0.8 nm, whereas the values for the non-primary cations (Co,Mg,Ni,Zn) range from 0.3–1.2 nm. For the Co-rich nanoparticles, the Co interface width ranges from 0.6 to 0.9 nm, with an average value of 0.7 nm, while the values of δ for the non-primary cations (Cu, Mg, Ni, Zn) range from 0.4 to 1.2 nm.

A 3D atomic reconstruction of all six elements in the nanocrystalline sample is seen in Fig. 3(b). Like the coarse-grained sample, the nanocrystalline sample displays Cu-rich nanoparticles throughout the observed volume. Unlike the coarse-grained sample, however, the nanocrystalline sample exhibits no signs of Co-rich regions. Regions enriched in Mg, Ni, Zn, and O are also not observed. To highlight the Cu-rich regions, isoconcentration surfaces were constructed from the region contained in the dashed black box in Fig. 3(b). The observed Cu-rich nanoparticles exhibit primarily non-spherical morphologies, with many nanoparticles exhibiting elongated or curved shapes [Fig. 4(d)]. The Cu-rich nanoparticles have an average diameter of 3.0 nm (radius of 1.5 nm).

A concentration proxigram of one of the Cu-rich nanoparticles in the nanocrystalline sample is seen in Fig. 4(e). The Cu-rich nanoparticles exhibit a diffuse compositional transition region, with the Cu concentration increasing from the outside to the center. Additionally, the Cu-rich nanoparticles are deficient, but not absent in the other four cations. The Cu-rich nanoparticles have an average Cu concentration of

34 at.%, which is slightly lower than the average concentration found in the coarse-grained sample (37 at.%). The average of the other cations is $M = 16$ at.%, while the oxygen concentration is 50 at.%. A summary of the composition details is presented in Fig. 5(b). Values for δ for the Cu-rich nanoparticles in the nanocrystalline sample, calculated using the proxigrams and Eqs. [1] and [2], range from 0.7 to 1.1 nm. The average value is 0.9 nm, which is thicker than the value for the Cu-rich nanoparticles in the coarse-grained sample (0.8 nm). The non-primary cations of the Cu-rich nanoparticles have δ values that range from 0.3 to 1.7 nm.

Thermodynamic modeling and phase stability

The software Thermo-Calc was used to model the equilibrium phase behavior in TM-ESO. As the Thermo-Calc oxide database does not currently contain data on ZnO, the quaternary equimolar (Co,Cu,Mg,Ni)O system was investigated instead. Thermo-Calc was used to investigate the stability of CuO tenorite as a function of temperature and composition by calculating the fraction of tenorite present between 200 and 900 °C and with Cu concentration ranging from 10 to 50 at.%. A heat map of temperature vs Cu concentration is presented in Fig. 6(a), with the colors representing the fraction of tenorite

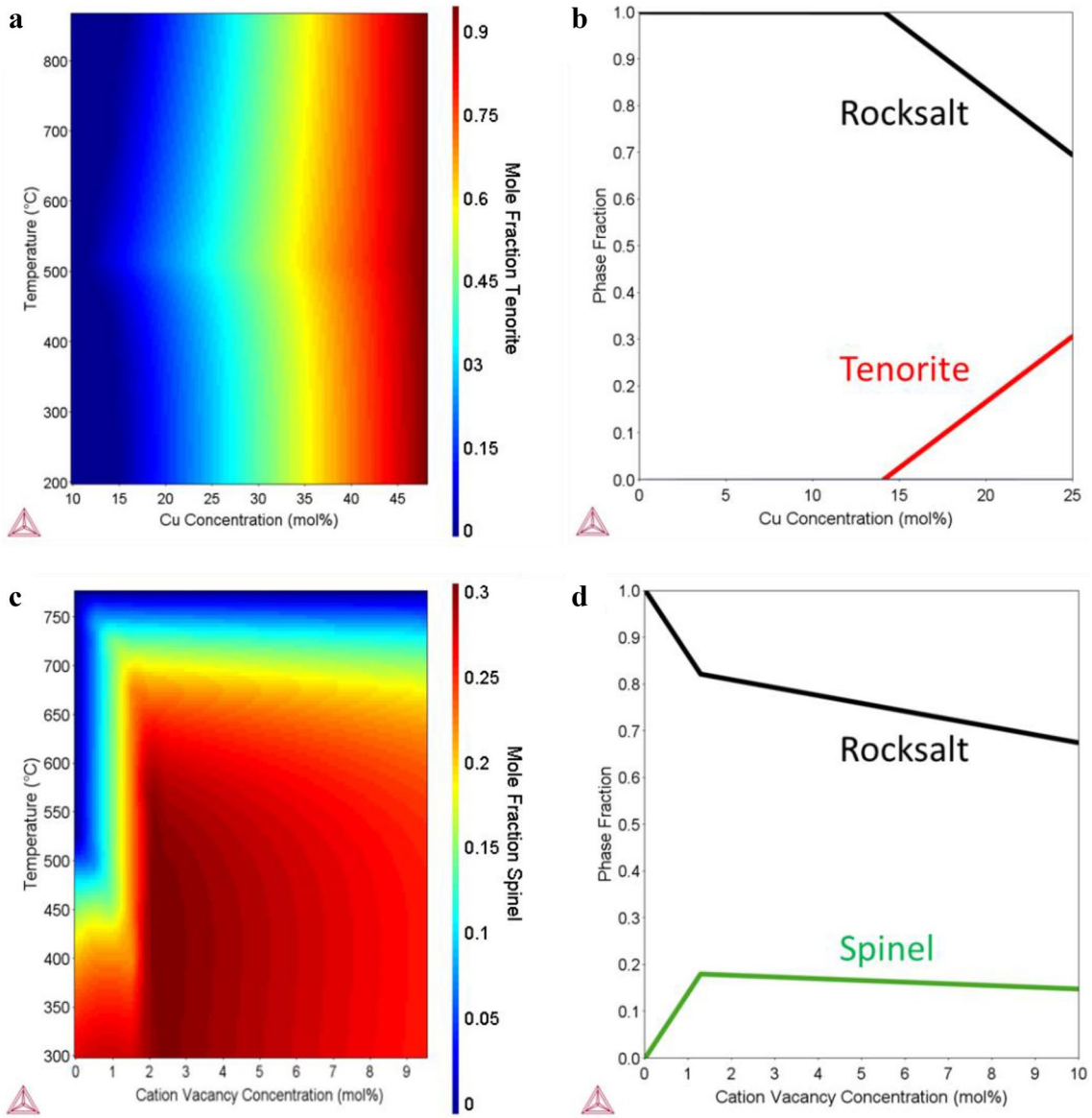

Figure 6: Role of composition and temperature on secondary-phase stability in (Co,Cu,Mg,Ni)O. (a) Heat map depicting the predicted phase fraction of tenorite (see color bar) stable at different temperatures and Cu concentrations. (b) The predicted phase fraction of tenorite stable at 700 °C with varying Cu concentrations. (c) Heat map depicting the predicted phase fraction of spinel stable at different temperatures and cation vacancy concentrations. (d) The predicted phase fraction of spinel stable at 700 °C with varying cation vacancy concentrations. All data were calculated using Thermo-Calc.

present. The fraction of tenorite predicted to form is highly sensitive to Cu concentration, with increasing Cu concentration leading to greater amounts of tenorite forming. Additionally, the calculations exhibit some temperature dependence of the tenorite formation. Thermo-Calc predicts that 520 °C is the temperature requiring the lowest Cu concentration to form the tenorite phase. Additionally, the tenorite stability becomes less sensitive to temperature with increasing Cu concentration.

Thermo-Calc predicts that at 700 °C the tenorite phase is highly sensitive to Cu concentration, [(Fig. 6(b)]. At the equimolar composition, Thermo-Calc predicts no tenorite formation at 700 °C. Instead, only the rocksalt phase is predicted at 700 °C. Further, tenorite is not predicted to form at Cu concentrations < 14 at.%. We note that behavior predicted by Thermo-Calc is contradicted by some of our previous experimental evidence. First, we do not experimentally observe the tenorite phase at temperatures ≥ 850 °C [11], which we propose is due to the entropic stabilization effect, which is not accounted for by Thermo-Calc. Second, we experimentally observe that the greatest fraction of tenorite emerges during heat treatment at 700 °C, with tenorite fraction decreasing at temperatures below 700 °C, which we propose is due to slower diffusion at lower temperature.

Unlike the tenorite phase, Thermo-Calc indicates that the formation of spinel in equimolar (Co,Cu,Mg,Ni)O is not sensitive to the concentration of any one specific cation (not shown). Instead, spinel stability is highly sensitive to cation vacancy concentration. A heat map of temperature vs cation vacancy concentration is presented in Fig. 6(c), with the colors representing the fraction of spinel present. The spinel phase tends to meaningfully form at cation vacancy concentrations > 1 at.%, and then declines at > 3 at.%. However, the spinel stability is highly temperature dependent, with lower temperatures predicting greater spinel stability at all cation vacancy concentrations. Additionally, Thermo-Calc predicts no spinel formation above 800 °C, which is consistent with our previous experimental results [12]. Thermo-Calc predicts that more spinel phase will form at lower temperatures, contradicting our experimental observations that the greatest fraction of spinel forms at 700 °C.

At 700 °C, Thermo-Calc predicts that the spinel phase is highly sensitive to cation vacancy concentration [Fig. 6(d)]. Similar to the tenorite phase, Thermo-Calc does not predict the formation of a spinel phase in equimolar (Co,Cu,Mg,Ni)O at 700 °C. The fraction of spinel predicted to form increases linearly with increasing cation vacancy concentration up to 1.8 at.% cation vacancy concentration. The spinel fraction is predicted to decrease linearly at cation vacancy concentrations > 1.8 at.%, due to the formation of an oxygen gas phase (not shown). It is known that cation vacancies play a role in spinel formation. For example, the rocksalt to spinel transformation in CoO is highly sensitive to vacancy concentration, with the transformation occurring at a critical vacancy concentration [22].

Thermo-Calc was used to calculate the thermodynamic values related to the phase transformation in the quaternary (Co,Cu,Mg,Ni)O. We use Thermo-Calc to estimate the interfacial energy (σ) and the driving force for the phase transformation (ΔG) for the rocksalt→tenorite/spinel phase transformations. We note that the oxygen concentration used in the rocksalt→spinel calculation is set to $O = 51$ at.%, which Thermo-Calc predicts will yield the greatest fraction of spinel phase. For the rocksalt→tenorite transformation, increasing Cu concentration leads to a decrease in σ [Fig. 7(a)] and an increase in ΔG [Fig. 7(b)] indicating that the formation of tenorite is more favorable as Cu concentration increases. In contrast, the rocksalt→spinel transformation exhibits a more complex relationship between cation concentration and the thermodynamic parameters. Increasing Co concentration results in a decline in σ up to ~ 30 mol% Co, with increasing Co concentrations resulting in an increase in σ (Fig. 7(d)]. ΔG for the rocksalt→spinel transformation generally increases with increasing Co concentration [Fig. 7(e)]. However, the trend in ΔG is non-monotonic due to the sensitivity of the spinel transformation on the non-primary cations (which decrease in concentration with increasing Co concentration).

Both σ and ΔG play a significant role in the nucleation of the secondary phases, making it difficult to interpret the role of composition on the phase transformation behavior when examining either thermodynamic variable individually. One way to account for the interplay between the two variables is to calculate the critical radius for nucleation (r^*) using [23]

$$r^* = \frac{3\sigma V}{\Delta G}, \tag{3}$$

where V is the molar volume of the transformed phase (calculated using Thermo-Calc). For the rocksalt→tenorite transformation, r^* decreases with increasing Cu concentration [Fig. 7(c)], which is consistent with the Thermo-Calc prediction that tenorite forms more readily with increasing Cu concentration [Fig. 6(b)]. For the rocksalt→spinel transformation, the predicted r^* decreases subtly with increasing Co concentration [Fig. 7(f)], indicating that the formation of spinel is not as strongly related to the cation concentration as the rocksalt→tenorite transformation. The range of values predicted by Thermo-Calc is summarized in Table 1. We note that the values of σ, ΔG, and r^* from Thermo-Calc are calculated from a very limited oxide thermodynamic database and are based on the quaternary (Co,Cu,Mg,Ni)O instead of the experimental composition of interest, (Co,Cu,Mg,Ni,Zn)O, because Zn is not in the database. As such, the *absolute values* of the three parameters are unlikely to be accurate. Notably, in this work, only the trends predicted by Thermo-Calc are

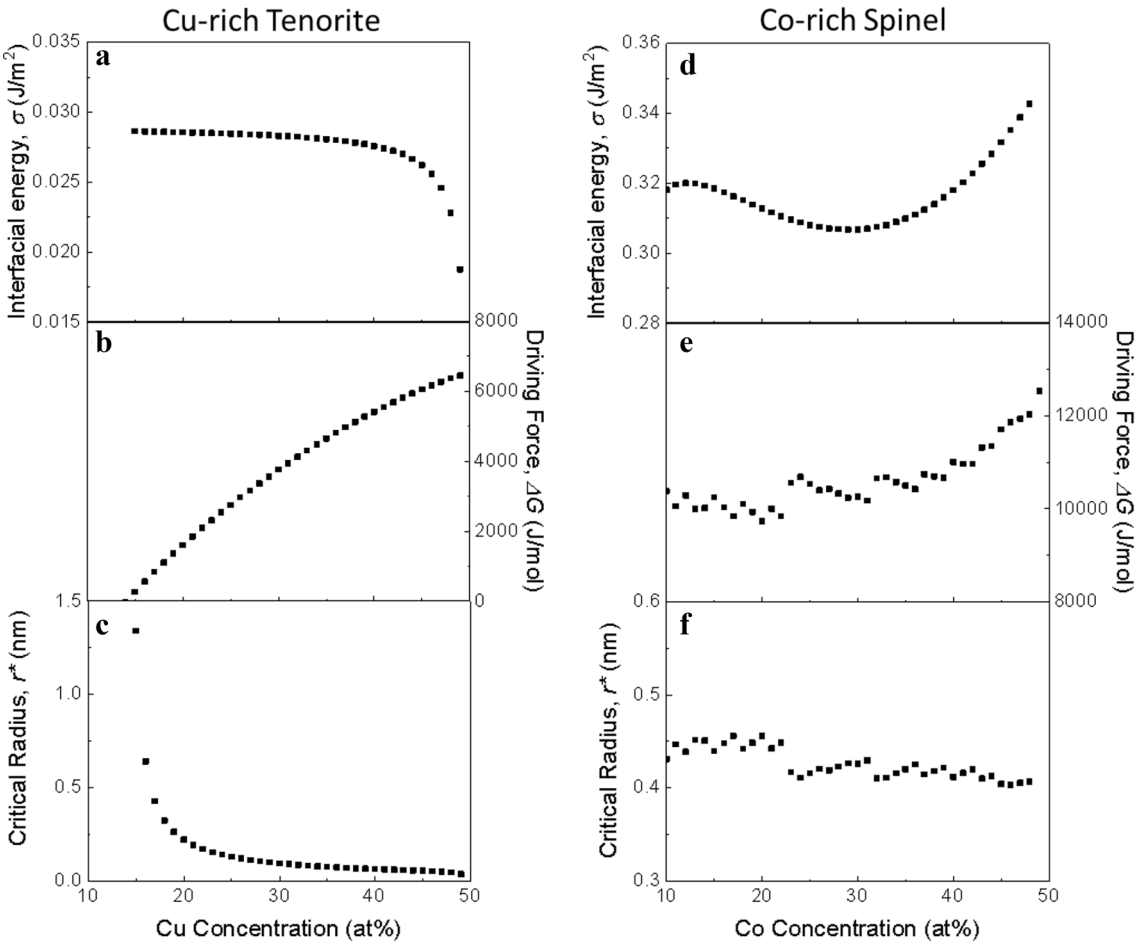

Figure 7: Role of composition on the phase transformation thermodynamic parameters in (Co,Cu,Mg,Ni)O. Calculated: (a) interfacial energy, σ, (b) the driving force for the phase transformation, ΔG, and (c) critical radius for nucleation, r^*, for the rocksalt→tenorite transformation. Calculated: (d) σ, (e) ΔG, and (f) r^*, for the rocksalt→spinel transformation in (Co,Cu,Mg,Ni)O with an oxygen concentration of 51 at.%. All data were calculated using Thermo-Calc.

TABLE 1: Summary of the calculated kinetic and thermodynamic parameters for Cu-rich tenorite and Co-rich spinel phase transformations in TM-ESO

	Thermo-Calc			LSW Model				Calderon et al. Model	
Phase	σ (J/m²)	ΔG (J/mol)	r^* (nm)	k (m³/s)	κ (s^{-1})	D (m²/s)	σ (J/m²)	ΔG (J/mol)	r^* (nm)
Cu-rich Tenorite	0.01–0.028	< 6500	0.03–1.3	3×10^{-26}	7	4.0×10^{-13}	11	550	38
Co-rich Spinel	0.32–0.34	10,000–12,500	0.4–0.45	8×10^{-27}	90	3.9×10^{-13}	2.5	324	16

The method/model used to calculate the values is listed in the headings.

considered, as they offer insight into the role of composition on the tenorite and spinel phase transformation. Therefore, to investigate the potential role of this database limitation on the overall Thermo-Calc trend predictions, the same analysis for the rocksalt→tenorite/spinel transformations was performed on the quinary (Ca,Co,Cu,Mg,Ni)O system (with Ca replacing Zn). Thermo-Calc predicts that the addition of Ca slightly decreases the minimum Cu concentration required to form tenorite, but otherwise does not change the trends observed in Fig. 6(a) and (b) (not shown). Similarly, the addition of Ca decreases the maximum amount of spinel that forms but does not change the trends in Fig. 6(c) and (d) (not shown). Thus, we observed minimal changes in the predicted thermodynamic parameters and identical trends with composition, verifying that this database

limitation and the application of four cations instead of five does not significantly influence the Thermo-Calc predictions.

Secondary-phase coarsening kinetics

Analysis of the temporal behavior of the phase transformation can provide insight into the nucleation and growth behavior of the secondary-phase particles. One of the most accessible models for describing how secondary-phase particles grow with time is the Lifshitz–Slyozov–Wagner (LSW) model. We note that the LSW model assumes a binary composition with an ideal dilute solid-solution primary phase and that the secondary-phase particles are spherical and consist of a single element [24]. TM-ESO meets none of these assumptions. Despite this, the LSW model provides a simple method of estimating kinetic parameters needed for more advanced calculations, without knowledge of the fundamental thermodynamic parameters. The LSW model has been successfully applied to other complex ceramics, such as (SiOC)-HfO_2 and SiZrCNO [25, 26].

From the LSW model, the kinetic rate constants k and κ can be calculated using [27]:

$$r^3 \approx kt, \tag{4}$$

$$f = f_e - \frac{(\kappa t)^{\frac{1}{3}}}{\Delta X}, \tag{5}$$

where r is the average particle radius, t is the heat treatment time, f is the mass fraction of the secondary phase, and f_e is the maximum possible fraction of secondary phase. Here, r was acquired from the dimensions of the secondary-phase particles using SEM/EDS, while the mass fractions were calculated from XRD and Rietveld refinement using MAUD [28]. Using the present work, as well as our previous work on TM-ESO [11–13], we can estimate the kinetic constants at 700 °C as follows: $k \approx 3 \times 10^{-26}$ m^3/s and $\kappa \approx 7$ s^{-1} for the rocksalt→tenorite transformation, while $k \approx 8 \times 10^{-27}$ m^3/s and $\kappa \approx 90$ s^{-1} for the rocksalt→spinel transformation. We emphasize that these values are estimations, as the available data on the phase transformation in TM-ESO are still limited. Despite this, our kinetic constants are reasonable compared to other materials at the same temperature (700 °C), such as 10^{-27} m^3/s for Ni alloys [24], 10^{-28} m^3/s for Cu–Co alloys [29], and 10^{-28} m^3/s for Cu–Fe alloys [30]. While the kinetic constants will be sensitive to temperature, the similarity to the kinetics constants found in literature for other materials gives confidence to our estimated values for TM-ESO.

The kinetic constants allow for the calculation of several meaningful values related to the growth of the secondary phases. For example, the effective diffusion coefficient for coarsening can be calculated from the LSW model using

$$D = \frac{9}{4}\left(k^2\kappa\right)^{\frac{1}{3}}. \tag{6}$$

From Eq. [6], $D = 4.0 \times 10^{-13}$ cm^2/s for the rocksalt→tenorite transformation and $D = 3.9 \times 10^{-13}$ cm^2/s for the rocksalt→spinel transformation. The nearly identical values for D between the two transformations, despite having different kinetic coefficients, imply that the dominant diffusion mechanism is the same between the two transformations. The LSW model assumes that the D in Eq. [6] should resemble the chemical (interdiffusion) coefficient, which is the diffusion behavior driven by a concentration gradient. Previous work on diffusion in TM-ESO indicates that the chemical diffusion coefficient is very similar to rocksalt structured CoO [31]. However, our estimated values of D are much lower than the estimated chemical diffusion coefficients for CoO and TM-ESO (8×10^{-8} cm^2/s at 700 °C), implying that the growth of the secondary phases is not strongly driven by a concentration gradient. Instead, we find that our estimated values for D are very similar to the self-diffusion coefficients (diffusion in the absence of a concentration gradient) of the constituent rocksalt oxides [32], in particular CoO (9.3×10^{-13} cm^2/s at 700 °C [33]), implying that the secondary-phase growth is dictated by cation self-diffusion in the primary rocksalt phase.

The LSW model can also be used to estimate σ:

$$\sigma = \frac{RT}{2X_m V}\left(\frac{k}{\kappa}\right)^{\frac{1}{3}}, \tag{7}$$

where R is the gas constant and T is the temperature (973 K). From Eq. [7], the LSW model estimates that $\sigma = 11$ J/m^2 for the rocksalt/tenorite interface and $\sigma = 2.5$ J/m^2 for the rocksalt/spinel interface. Both values are significantly higher than the those predicted by Thermo-Calc (Table 1), indicating that Thermo-Calc underestimates the difficulty of forming a new interface for the secondary phase. Additionally, our estimated interface energies are higher than those seen in literature for other materials at similar temperatures, such as 0.02–0.1 J/m^2 for Ni-based superalloys [24], 0.55 J/m^2 for Fe-Cu alloys [30], and 0.15 J/m^2 for Cu–Co alloys [29]. Low σ values indicate a resistance to particle coarsening, instead favoring the formation of a fine distribution of secondary phases, which are used for improving the strength of alloys [34]. The relatively high σ values in TM-ESO illustrate the difficulty of nucleating the secondary phases and the preference for particle coarsening.

Calderon et al. modified the LSW model to remove the assumption that the primary phase be a dilute solid solution and the secondary phase a pure element [35]. From the Calderon model, the kinetic rate constants Eqs. [4] and [5] can be related to σ and ΔG with

$$\left(\frac{k}{\kappa}\right)^{\frac{1}{3}} = \frac{2\sigma V \Delta X f_e}{\Delta G}. \quad (8)$$

It is important to note that the σ value in Eq. [8] is different from Eq. [7], meaning that Eq. [8] requires an accurate thermodynamic model of σ or ΔG to calculate the other. It has been observed that σ values from the Calderon model are an order of magnitude smaller than those from the LSW model. We therefore estimate ΔG for the phase transformations in TM-ESO by using σ values that are one order of magnitude smaller than the ones we calculated using the LSW model. From Eq. [8], we estimate $\Delta G \approx 550$ J/mol for the rocksalt→tenorite transformation and $\Delta G \approx 324$ J/mol for the rocksalt→spinel transformation. These values are one to two orders of magnitude smaller than those predicted by Thermo-Calc, indicating that Thermo-Calc underestimates the driving force for the phase transformations.

Discussion

Pre-nucleation environment

The existence of both large secondary-phase particles with sizes > 40 nm (observed with SEM) and nanoparticles with sizes ≤ 3 nm (observed with APT) indicates that the Cu-rich and Co-rich phases experience simultaneous nucleation and growth processes during heat treatment [36]. Our Thermo-Calc calculations predict that the formation of the tenorite and spinel phases are closely related to the local composition (Fig. 6). Specifically, Thermo-Calc predicts that the tenorite phase forms when the composition of TM-ESO is enriched in Cu, while the spinel phase forms when there are cation vacancies. Local concentration fluctuations are known to form in materials with random solid-solution structures [37]. Our Thermo-Calc predictions imply that local regions that are enriched or deficient in cations could act as nucleation sites for the formation of secondary phases. Such a phenomenon has been observed in ceramics before, such as spinel phases precipitating on cation vacancies in Fe–NiO and Ti–MgO [38, 39].

In our previous work, we studied the chemical homogeneity of the as-sintered, single-phase TM-ESO samples using APT, finding that the as-sintered TM-ESO samples had no obvious secondary phases at the nanoscale [18]. However, binomial frequency analysis revealed that the as-sintered TM-ESO samples had a non-random cation distribution, likely due to local regions that are enriched in one or more cations [40]. We observed that the single-phase TM-ESO samples exhibit local Cu concentrations as high as 14 at.% and cation vacancy concentrations as high as 3 at.% [18]. These local concentration fluctuations can act as sites for nucleation and enable continuous nucleation of secondary phases during heat treatment [41, 41]. We propose that the local concentration fluctuations present in the non-heat-treated, single-phase TM-ESO samples will act as nucleation sites for the Cu-rich and Co-rich secondary phases.

Precursor-phase nucleation

In materials where the crystal structure of the primary phase and secondary phase differs significantly, there will be a large interfacial energy, and thus a large barrier to nucleation [36]. In many materials, this barrier to nucleation is circumvented by the nucleation of a *transitionary precursor phase* with a similar crystal structure to the primary phase [36]. The formation of transitionary precursor phases is frequently seen during precipitation, with the formation of Guinier–Preston (GP) zones and other precursor phases in Al and Cu alloys being well studied [36]. Precursor-phase nucleation has even been seen in ceramics, such as the formation of precursor phases before the nucleation of Al_2O_3 in non-stoichiometric $MgAl_2O_4$ [43], or the formation of GP zones before the nucleation of spinel in Ti–MgO [39].The advent of APT greatly facilitates the identification of these precursor phases by allowing for the accurate measurement of composition at the nanoscale. Precursor phases can often be identified by observing particles whose composition deviates from the expected equilibrium chemistry of the secondary phases measured at larger length scales. For example, APT was used in intermetallic TiAl to identify the ω'' precursor phase which forms before the nucleation of ω_o precipitates [44], and in an Al–Cu–Mg–Ag alloy where the formation of GP zones and other precursors form before the formation of Ω and θ' phases [45].

Using APT, we have confirmed that the Cu-rich and Co-rich nanoparticles are not single-cation oxides, but are instead multi-cation oxides enriched in a primary element. The Cu-rich nanoparticles in the coarse-grained sample possess an average non-primary cation concentration of Co = 3.4 at.%, Mg = 3.2 at.%, Ni = 3.0 at.%, and Zn = 3.4 at.%. The solubility limits for Co, Mg, Ni, and Zn, in CuO tenorite are known to be approximately 2.5, 2.0, 1.0, and 2.0 at.%, respectively [46–49]. Our observed cation concentrations are close to their respective individual solubility limits. Similar results are observed for the Cu-rich nanoparticles in the nanocrystalline sample, with non-primary cation concentrations of Co = 4.2 at.%, Mg = 3.6 at.%, Ni = 4.6 at.%, and Zn = 3.7 at.%. On average, the non-primary cation concentration in the Cu-rich phase is higher in the nanocrystalline sample compared to the coarse-grained sample. However, the nanocrystalline sample is heat treated at a lower temperature and for a shorter time (550 °C for 2 h) compared to the coarse-grained sample (700 °C for 12 h). Notably, the above-listed solubility limits for Co, Mg, Ni, and Zn, in CuO tenorite are only the individual cation solubility limits. Therefore, the observed non-primary cation

concentration ($M = 13$ at.%) is unexpectedly high, indicating that the Cu-rich phase in TM-ESO can accommodate significantly more non-primary cations than CuO tenorite would be expected to. We propose that the Cu-rich nanoparticles observed in APT are not a Cu-rich tenorite phase but are instead a Cu-rich multicomponent transition phase acting as a precursor to tenorite.

There are two primary types of Co-based spinel oxides: Co_3O_4 and MCo_2O_4. Rocksalt CoO will oxidize to form Co_3O_4 (Co = 43 at.%, O = 57 at.%) at 600–900 °C in air. Co will also react to form MCo_2O_4 (Co = 29 at.%, M = 14 at.%, O = 57 at.%), where M = Co,Mg,Ni,Zn, at > 550 °C [50]. However, the Co-rich nanoparticles observed in APT exhibit an average composition of Co = 33 at.%, M = 16 at.%, O = 51 at.%, which deviates from both possible Co spinel variants. Like the Cu-rich phase, we propose that the observed Co-rich nanoparticles in APT are not a Co-rich spinel phase but are instead a Co-rich multicomponent transition phase acting as a precursor to spinel.

The existence of the precursor phase can be verified by considering the critical radius for nucleation, r^*. Thermo-Calc predicts that $r^* < 1$ nm for each of the secondary phases [Fig. 7(c) and (f)]. While Thermo-calc provides valuable insights about the role of composition on the phase transformations, our kinetic analysis indicates that Thermo-Calc underestimates the difficulty of nucleating the secondary phase. From the Calderon model [35], r^* can be elegantly calculated without knowledge of σ or ΔG using

$$r^* = \frac{3}{2 f_e \Delta X} \left(\frac{k}{\kappa} \right)^{\frac{1}{3}}. \quad (9)$$

Using Eq. [9], we calculate $r^* = 38$ nm for the rocksalt→tenorite transformation and $r^* = 16$ nm for the rocksalt→spinel transformation. These values for r^* are larger than the size of the nanoparticles observed in APT for both phases (each on the order of 2 nm), indicating that the Cu-rich and Co-rich nanoparticles are not, yet, the Cu-rich tenorite and Co-rich spinel secondary phases that we observe in XRD and SEM. Thus, the r^* values calculated from our kinetic constants provide further support for our hypothesis that the nanoparticles observed in APT are actually precursor phases.

Differences in crystal structure between a primary phase and secondary phase will lead to coherency strains and a large interfacial energy, limiting nucleation of the secondary phase [36]. The formation of precursor phases in TM-ESO is logical considering the difference in crystal structure between the cubic rocksalt, the monoclinic tenorite, and the cubic spinel phases. While the rocksalt and spinel phases are both cubic, our XRD results indicate that the spinel phase has a much larger lattice parameter (8.1 Å) than the rocksalt phase (4.23 Å), indicating that coherency strains and a large interfacial energy are still expected between the two phases. Our precursor phase likely adopts a crystal structure that is intermediate between the rocksalt and secondary phases. Having a crystal structure similar to the rocksalt phase will reduce the coherency strains and interface energy for the precursor phase, thus reducing the barrier for nucleating the secondary phases.

Our calculated r^* values for the rocksalt→tenorite/spinel transformations indicate that the nanoparticles observed in APT are not tenorite or spinel, leading to the hypothesis that they are instead precursor phases. Complete validation for this hypothesis would require the calculation of r^* values for the precursor phases, for which the necessary information currently does not exist. Accurate values for r^* cannot be predicted using Thermo-Calc as there is not sufficient thermodynamic data for the precursor phases. Acquiring the necessary experimental information to calculate r* will also be very challenging for three reasons, but could be explored in future work. First, the secondary phases in TM-ESO grow rapidly with heat treatment, necessitating very careful control of the heat treatment conditions to avoid transforming the precursor phases into tenorite or spinel. Second, the precursor phases are very small and will require detailed APT observations for each heat treatment condition. Third, the secondary phases in TM-ESO continuously nucleate. New precursor phases will emerge simultaneously with the coarsening of existing phases, making it difficult to determine the evolution in precursor phase size. Despite being unable to calculate r^* for the precursor phases, our APT observations, thermodynamic modeling, kinetic calculations, as well as precedence from the literature, give us confidence in our hypothesis that the observed nanoparticles are precursor phases.

Precursor-phase evolution

From our kinetics analysis, we have determined that the effective diffusivity is very similar to the self-diffusion behavior of other rocksalt oxides. The growth of the tenorite and spinel particles is dictated by the diffusion of cations in the primary rocksalt phase. However, at very small particle sizes the growth of secondary phases will be influenced by the diffusion behavior in three regions: the primary phase, the secondary phase, and the compositional transition region between the two phases [51]. Our APT analysis can shed light on the diffusion in the precursor phases. During the growth of the precursor phase, the primary cations move from the primary rocksalt phase into the precursor phase, while the non-primary cations move in the opposite direction. At small nanoparticle sizes, δ for the individual cations will be highly dependent on the diffusion behavior of the cations as they migrate to their destination. Cations with smaller δ values can be assumed to diffuse more quickly than those with larger δ values. Here, we

use our calculated cation δ values as a proxy for the diffusion behavior.

Self-diffusion of cations in rocksalt oxides has been well studied, with the diffusion of cations being closely related to their ionic radii and polarizability, as well as the defect chemistry of the oxide [32]. The diffusion behavior of the five cations in TM-ESO has been previously measured in single-crystal MgO at temperatures > 1000 °C [52, 52]. The calculated diffusivity values of the cations in MgO at 700 °C and 550 °C follow the order Zn > Co > Cu > Ni > Mg. Therefore, the expected values for the interface width, δ, in precursor-phase nanoparticles whose diffusion behavior is like a rocksalt oxide would follow the trend Mg > Ni > Cu > Co > Zn. We note that the diffusivities of Co, Cu, and Ni in MgO are similar (within the same order of magnitude), so a trend in δ of Mg > Co ~ Cu ~ Ni > Zn is reasonable. Of the five constituent oxides in TM-ESO, MgO has been the most well studied. However, the diffusion of the cations in TM-ESO has also been studied in some of the other constituent oxides, such as NiO, and found to follow similar behavior to cations in MgO [54].

In the coarse-grain sample (heat treated at 700 °C), the average values of δ for the Cu-rich and Co-rich nanoparticles follow a trend of Mg > Co > Cu > Ni > Zn [Fig. 5(b)]. Mg has the highest average δ value, Zn the lowest, while Co, Cu, and Zn are similar. The trend in δ values is similar to what would be expected for cation diffusion in rocksalt oxides, indicating that both precursor phases have a rocksalt-like crystal structure. In the nanocrystalline sample (heat treated at 550 °C), the average values of δ for the Cu-rich nanoparticles follow a trend of Co > Mg > Cu > Ni > Zn, indicating that Co is the slowest moving cation in this situation instead of Mg. We propose that the deviation from the behavior in the coarse-grain sample is related to the low heat treatment temperature used for the nanocrystalline sample. Self-diffusion experiments in rocksalt oxides are rarely performed below 1000 °C due to the time required to generate meaningful self-diffusion. However, diffusion mechanisms for cations in rocksalt oxides are often different at different temperatures, leading to significant deviations in diffusivity from values extrapolated from high temperatures. Cations in rocksalt oxides diffuse through a cation vacancy mechanism, with the concentration and types of vacancies being sensitive to temperature [55]. For example, the activation energy for diffusion of Co and Cr in MgO changes at temperatures < 1000 °C due to a change in vacancy bonding energy [56]. However, TM-ESO is known to have a complex defect structure [31], with more work needing to be done to understand how this defect structure changes with temperature.

Our analysis indicates that the diffusion behavior of the cations into and out of the precursor phases resembles the behavior of cations in a rocksalt phase. We therefore propose that the precursor phases have a rocksalt-like structure and corresponding diffusion behavior. However, the interface itself can influence the diffusion behavior. In their foundational study, Ardell and Ozolins found that the growth of small secondary-phase particles is significantly influenced by the interface between the particle and primary phase due to the interface operating as a diffusion bottleneck [51]. The interface possesses its own distinct diffusion coefficient, D_I, which can be calculated using $D_I = 2(DD_p)/(D + D_p)$, where D_p is the diffusion coefficient of the secondary phase. However, given that the diffusion behavior of our precursor phases resembles a rocksalt-like phase, $D_I \approx D \approx D_p$. The interface only meaningfully influences the growth of small particles when $r << \delta D/D_I$, which does not hold for the precursor-phase nanoparticles in TM-ESO. We conclude that the growth of the precursor phases can be described primarily by the cation diffusion behavior in rocksalt oxides.

Transformation sequence

At a certain particle size, the activation barrier for transformation will be low enough that the precursor phase will transform into tenorite or spinel. There are several mechanisms that can lead to the formation of secondary phases from precursor phases. For example, in TiAl alloys and Al–Cu–Mg alloys, the formation of multiple consecutive precursor phases gradually reduces the activation barrier for transformation due to changes in local concentration and local distortions in the lattice [44, 45]. Alternatively, in some Al–Cu and Al–Ag alloys, the secondary phases form because of a separate distinct nucleation event, which is stimulated by defects (such as dislocations or vacancies) and the primary/precursor interfaces that form as a result of the precursor phases [36]. However, our Thermo-Calc results indicate that the activation barrier for transformation is dependent on composition, with the conditions for the formation of tenorite and spinel becoming more favorable as the concentration of the primary cation increases. We hypothesize that the increasing primary cation concentration in the precursor phases will partially contribute to the eventual transformation into Cu-rich tenorite and Co-rich spinel secondary phases.

We cannot unambiguously determine the mechanism that causes the precursor→tenorite/spinel transformation. However, our observations and calculations indicate that the behavior of TM-ESO is similar to conventional oxides, indicating that insights into the nature of these transformation can be acquired from literature on more established oxides. Previous work has shown that ultrathin films of CuO can form in a rocksalt structure under specific processing conditions [57]. This rocksalt structure has a tetragonal symmetry due to

the existence of a Jahn–Teller structural distortion [58]. However, in the absence of an additional stabilization mechanism (such as other cations on the sublattice [59]), CuO is unstable against this Jahn–Teller distortion, leading to a structural transformation to the equilibrium tenorite structure [60]. We hypothesize that the transformation from Cu-rich rocksalt-like precursor phase to Cu-rich tenorite secondary phase in TM-ESO occurs through a similar structural distortion-based phase transformation. Once transformed, the Cu-rich tenorite particles continue to coarsen with increasing heat treatment time. In the coarse-grained samples, the tenorite particles transform from a sphere-like morphology to a needle-like morphology [Fig. 2(a)] and finally to a plate-like morphology as the particle grows due to misfit strain effects [13]. Conversely, confinement from the grain boundaries causes the tenorite particles to encompass an entire grain in the nanocrystalline samples [Fig. 2(b)] [11].

Spinel phases possess two dedicated cation sublattices, making the precursor→spinel transformation more complicated than the precursor→tenorite transformation. Rocksalt→spinel transformations have been observed before in other materials, such as Sn–CoO and Ti–MgO [39, 61]. The transformation occurs when a critical concentration of cation interstitials and vacancies is reached, leading to a collapse of the rocksalt structure and the rearrangement of the atoms [62]. Spinel phases often nucleate on dislocations as well as vacancy and defect clusters in rocksalt oxides [61]. However, many spinel nucleation events are preceded by the formation of a precursor phase that nucleates on cation vacancies, such as in Ti–MgO and Zr–TiO_2 [39, 63]. Continued diffusion and cation vacancy/interstitial formation in the precursor phase will lead to the defect arrangements necessary to complete the spinel transformation. We therefore hypothesize that the transformation from Co-rich rocksalt-like precursor to Co-rich spinel secondary phase in TM-ESO proceeds through a similar defect-mediated transformation. In contrast to the Cu-rich tenorite phase, after transformation, the Co-rich spinel phase exhibits minimal misfit strain with the primary rocksalt phase and maintains its sphere-like morphology as it coarsens [13].

Using APT, Thermo-Calc modeling, and kinetic analysis, we provide insight into the nucleation and growth behavior of the secondary phases in TM-ESO. A schematic summary of the secondary-phase nucleation sequence is seen in Fig. 8. Direct nucleation of the secondary phases is not thermodynamically favorable in equimolar TM-ESO. Instead, local regions of enrichment in Cu or cation vacancies stimulate the nucleation of the Cu-rich and Co-rich phases, respectively. However, there is a significant barrier to nucleation of the Cu-rich tenorite and Co-rich spinel secondary phases directly. We propose that

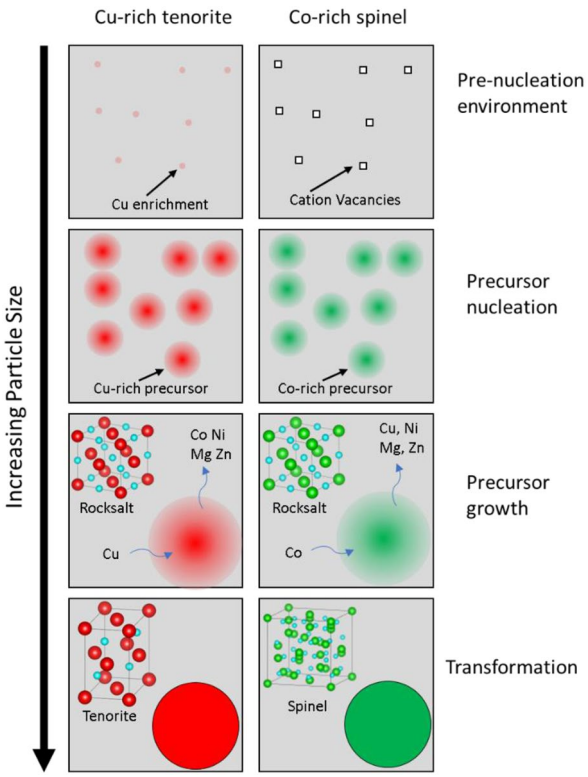

Figure 8: Nucleation and growth of the tenorite and spinel phases in TM-ESO. Schematic illustrating the nucleation, growth, and transformation sequence for the Cu-rich tenorite and Co-rich spinel phases, respectively, in TM-ESO. Straight arrows mark labeled regions; wavy arrows denote cation diffusion.

TM-ESO nucleates Cu-rich and Co-rich precursor phases with a rocksalt-like structure. These precursor phases then transform to the tenorite or spinel secondary phases through distinct transformation mechanisms.

Conclusions

APT, Thermo-Calc modeling, and kinetic analysis were used to investigate the nucleation and growth behavior of the Cu-rich tenorite and Co-rich spinel secondary phases in TM-ESO. Bulk coarse-grained and nanocrystalline TM-ESO samples were heat treated to induce the formation of secondary phases. XRD and SEM/EDS verify that both samples possess a micro-scale multi-phase state, with the coarse-grained sample containing both a tenorite and a spinel secondary phase, and the nanocrystalline sample containing the tenorite secondary phase. APT of the two samples reveals the presence of Cu-rich and Co-rich multicomponent nanoparticles that are ~ 2 nm in size. Thermo-Calc predicts that the formation of the secondary phases is highly composition dependent, while kinetic analysis reveals that the r^* for the

secondary-phase formation is larger than the nanoparticles observed in APT. From the experimental results and calculations, we can make the following statements about the nucleation and growth behavior.

1. The Cu-rich phase nucleates in regions with Cu enrichment, while the Co-rich phase nucleates in regions with cation vacancies.
2. The tenorite and spinel phases do not nucleate directly. Instead, Cu-rich and Co-rich precursor phases nucleate first.
3. The diffusion behavior in the precursor phases implies that they possess a rocksalt-like structure and behavior.
4. The precursor→tenorite transformation occurs through a structural distortion-based transformation, while the precursor→spinel transformation occurs through a defect-mediated transformation
5. The growth of the tenorite and spinel secondary phases is dictated by cation diffusion in the primary rocksalt phase. Simultaneously, there is a continuous nucleation of new precursor-phase nanoparticles.

Our work provides fundamental insights into the nucleation and growth behavior of secondary phases in TM-ESO. We find that TM-ESO has similar diffusion behavior to other rocksalt oxides, and it follows established kinetic and phase nucleation models. Although ESOs have many unique features, their secondary-phase formation behavior is similar to many conventional oxides. These insights will be instrumental when engineering the microstructure of ESO materials in the pursuit of specific applications and functionalities.

Methods

TM-ESO powders were prepared from constituent oxide nanopowders using solid-state methods. CoO (50 nm reported particle size, 99.7 wt% purity), CuO (25–55 nm), MgO (50 nm, 99.95%), 99.95%), NiO (18 nm, 99.98%), and ZnO (18 nm, 99.95%) nanopowders were sourced from US Research Nanomaterials. The oxide nanopowders were blended using a Fritsch Premium 7 planetary ball mill (PBM) at 300 rpm for 3 h using silicon nitride jars and milling media. These powders were heat treated at 900 °C for 20 min to complete the solid-state reaction and form single-phase TM-ESO powder [11]. These fully reacted powders were reground at 300 rpm for 12 h in the PBM. Coarse-grained samples were consolidated using conventional sintering with a CM Furnaces 1210BL elevator furnace at 1100 °C for 12 h. Nanocrystalline samples were consolidated using a Fuji model 825S SPS instrument. Consolidation was performed by heating to 700 °C at 200 °C/min and holding for 5 min. Additional information about powder synthesis and consolidation can be found in our previous work [11].

Heat treatment was performed using the above-mentioned elevator furnace. Coarse-grained samples were heat treated at 700 °C for 12 h; nanocrystalline SPS-consolidated samples were heat treated at 550 °C for 2 h. The heat-treated samples were polished using diamond slurry down to 1 μm. Archimedes method was used to measure the density of the coarse-grained and nanocrystalline TM-ESO samples. All samples exhibited a relative density of ≥ 98% before heat treatment.

The macroscopic phase state of the samples was measured using a Rigaku Ultima III XRD instrument. The microstructure of the bulk samples was examined on fracture surface specimens using a Hitachi Regulus 8230 SEM. EDS maps were collected on polished samples using a Bruker Flatquad EDS instrument. An accelerating voltage of 3 kV was used during EDS measurements, which we have shown to yield the spatial resolution necessary to visualize the small (< 100 nm) secondary-phase features in TM-ESO [11]. Fracture surface specimens were used to measure the average grain size.

A Zeiss Auriga 60 focused ion beam (FIB) system was used to prepare needle-shaped APT specimens from both the consolidated coarse-grained and nanocrystalline heat-treated samples. The region of interest was protected from Ga ion damage using a 150-nm-thick platinum capping layer. Annular milling was used to create the needle-shaped specimens with a tip diameter of < 100 nm. APT measurements were carried out at 50 K using a Cameca LEAP 4000X HR. Sample ablation was performed using a pulsed laser with a wavelength of 355 nm, a pulse energy of 60 pJ, and a pulse frequency of 100 kHz. Analysis was performed using Cameca's integrated visualization and analysis software (IVAS).

Thermo-Calc 2021b was used to investigate the equilibrium phase behavior of TM-ESO as a function of temperature and composition [64]. The "Property Model Calculator" function was used to estimate the driving force for segregation (ΔG) and the gradient energy (σ) for the various segregation scenarios. The TCXO v11 oxide database was used as the source of the thermodynamic data for the calculations. We note that the TCXO database currently does not support Zn or ZnO. Therefore, the quaternary (Co,Cu,Mg,Ni)O system was investigated instead.

Acknowledgments

The authors acknowledge the use of facilities and instrumentation at the UC Irvine Materials Research Institute (IMRI), which is supported in part by the National Science Foundation (NSF) through the UC Irvine Materials Research Science and Engineering Center (DMR-2011967). The authors are grateful

to the Karlsruhe Nano Micro Facility (KNMF) for support and access to APT and FIB facilities. Partial support was provided by NSF under award CMMI-2029966. This work was also partially supported by the UC Irvine MRSEC, Center for Complex and Active Materials, under NSF award DMR-2011967. Authors acknowledge the support of the software and databases from the Thermo-Calc Software company through the ASM Materials Genome Toolkit Award.

Data availability

The raw/processed data required to reproduce these findings cannot be shared at this time as the data also form part of an ongoing study.

Declarations

Conflict of interest The authors declared that they have no conflict of interest to this work. We declare that we do not have any commercial or associative interest that represents a conflict of interest in connection with the work submitted.

Open Access

References

1. C.M. Rost, E. Sachet, T. Borman, A. Moballegh, E.C. Dickey, D. Hou, J.L. Jones, S. Curtarolo, J.P. Maria, Entropy-stabilized oxides. Nat. Commun. **6**, 8485 (2015)
2. S. Akrami, P. Edalati, M. Fuji, K. Edalati, High-entropy ceramics: Review of principles, production and applications. Mater. Sci. Eng. R **146**, 100644 (2021). https://doi.org/10.1016/j.mser.2021.100644
3. D. Bérardan, S. Franger, D. Dragoe, A.K. Meena, N. Dragoe, Colossal dielectric constant in high entropy oxides. Phys. Status Solidi - Rapid Res. Lett. **10**, 328–333 (2016). https://doi.org/10.1002/pssr.201600043
4. A. Sarkar, L. Velasco, D. Wang, Q. Wang, G. Talasila, L. de Biasi, C. Kübel, T. Brezesinski, S.S. Bhattacharya, H. Hahn, B. Breitung, High entropy oxides for reversible energy storage. Nat. Commun. **9**, 3400 (2018). https://doi.org/10.1038/s41467-018-05774-5
5. S.H. Albedwawi, A. AlJaberi, G.N. Haidemenopoulos, K. Polychronopoulou, High entropy oxides-exploring a paradigm of promising catalysts: a review. Mater. Des. **202**, 109534 (2021). https://doi.org/10.1016/j.matdes.2021.109534
6. A. Sarkar, R. Djenadic, N.J. Usharani, K.P. Sanghvi, V.S.K. Chakravadhanula, A.S. Gandhi, H. Hahn, S.S. Bhattacharya, Nanocrystalline multicomponent entropy stabilised transition metal oxides. J. Eur. Ceram. Soc. **37**, 747–754 (2017). https://doi.org/10.1016/j.jeurceramsoc.2016.09.018
7. H. Guo, X. Wang, A.D. Dupuy, J.M. Schoenung, W.J. Bowman, Growth of nanoporous high-entropy oxide thin films by pulsed laser deposition. J. Mater. Res. **37**, 124–135 (2022). https://doi.org/10.1557/s43578-021-00473-2
8. A.L. Vyatskikh, B.E. MacDonald, A.D. Dupuy, E.J. Lavernia, J.M. Schoenung, H. Hahn, High entropy silicides: CALPHAD-guided prediction and thin film fabrication. Scr. Mater. **201**, 113914 (2021). https://doi.org/10.1016/j.scriptamat.2021.113914
9. J. Gild, Y. Zhang, T. Harrington, S. Jiang, T. Hu, M.C. Quinn, W.M. Mellor, N. Zhou, K. Vecchio, J. Luo, High-entropy metal Diborides: a new class of high-entropy materials and a new type of ultrahigh temperature ceramics. Sci. Rep. **6**, 37946 (2016). https://doi.org/10.1038/srep37946
10. P. Sarker, T. Harrington, C. Toher, C. Oses, M. Samiee, J.-P. Maria, D.W. Brenner, K.S. Vecchio, S. Curtarolo, High-entropy high-hardness metal carbides discovered by entropy descriptors. Nat. Commun. **9**, 4980 (2018). https://doi.org/10.1038/s41467-018-07160-7
11. A.D. Dupuy, X. Wang, J.M. Schoenung, Entropic phase transformation in nanocrystalline high entropy oxides. Mater. Res. Lett. **7**, 60–67 (2019). https://doi.org/10.1080/21663831.2018.1554605
12. A.D. Dupuy, I.-T. Chiu, P. Shafer, E. Arenholz, Y. Takamura, J.M. Schoenung, Hidden transformations in entropy-stabilized oxides. J. Eur. Ceram. Soc. **41**, 6660–6669 (2021). https://doi.org/10.1016/j.jeurceramsoc.2021.06.014
13. A.D. Dupuy, J.M. Schoenung, Morphological evolution in nanostructured secondary phases in entropy stabilized oxides. Mater. Charact. **15**, 112301 (2022). https://doi.org/10.1016/j.matchar.2022.112301
14. D.N. Seidman, Three-dimensional atom-probe tomography: advances and applications. Annu. Rev. Mater. Res. **37**, 127–158 (2007). https://doi.org/10.1146/annurev.matsci.37.052506.084200
15. Z. Fu, A. Hoffman, B.E. MacDonald, Z. Jiang, W. Chen, M. Arivu, H. Wen, E.J. Lavernia, Atom probe tomography study of an $Fe_{25}Ni_{25}Co_{25}Ti_{15}Al_{10}$ high-entropy alloy fabricated by

powder metallurgy. Acta Mater. **179**, 372–382 (2019). https://doi.org/10.1016/j.actamat.2019.08.047

16. K.G. Pradeep, N. Wanderka, P. Choi, J. Banhart, B.S. Murty, D. Raabe, Atomic-scale compositional characterization of a nanocrystalline AlCrCuFeNiZn high-entropy alloy using atom probe tomography. Acta Mater. **61**, 4696–4706 (2013). https://doi.org/10.1016/j.actamat.2013.04.059
17. M.R. Chellali, A. Sarkar, S.H. Nandam, S.S. Bhattacharya, B. Breitung, H. Hahn, L. Velasco, On the homogeneity of high entropy oxides: an investigation at the atomic scale. Scr. Mater. **166**, 58–63 (2019). https://doi.org/10.1016/j.scriptamat.2019.02.039
18. A.D. Dupuy, M.R. Chellali, H. Hahn, J.M. Schoenung, Multi-scale phase homogeneity in bulk nanocrystalline high entropy oxides. J. Eur. Ceram. Soc. **41**, 4850–4858 (2021). https://doi.org/10.1016/j.jeurceramsoc.2021.03.035
19. O.C. Hellman, J.A. Vandenbroucke, J. Rüsing, D. Isheim, D.N. Seidman, Analysis of three-dimensional atom-probe data by the proximity histogram. Microsc. Microanal. **6**, 437–444 (2000). https://doi.org/10.1007/S100050010051
20. F. Forghani, J.C. Han, J. Moon, R. Abbaschian, C.G. Park, H.S. Kim, M. Nili-Ahmadabadi, On the control of structural/compositional ratio of coherent order-disorder interfaces. J. Alloys Compd. **777**, 1222–1233 (2019). https://doi.org/10.1016/j.jallcom.2018.10.128
21. A.J. Ardell, Gradient energy, interfacial energy and interface width. Scr. Mater. **66**, 423–426 (2012). https://doi.org/10.1016/j.scriptamat.2011.11.043
22. J.T. Cox, C.M. Quinn, Some aspects of the role of the cation vacancy density in the phase transition from monoxide to spinel in the lithium-cobalt-oxygen system. Mater. Res. Bull. **4**, 165–170 (1969). https://doi.org/10.1016/0025-5408(69)90052-X
23. T. Philippe, D. Blavette, P.W. Voorhees, Critical nucleus composition in a multicomponent system. J. Chem. Phys. **141**, 124306 (2014). https://doi.org/10.1063/1.4896222
24. A.J. Ardell, A1–L12 interfacial free energies from data on coarsening in five binary Ni alloys, informed by thermodynamic phase diagram assessments. J. Mater. Sci. **46**, 4832–4849 (2011). https://doi.org/10.1007/s10853-011-5395-x
25. H.-J. Kleebe, K. Nonnenmacher, E. Ionescu, R. Riedel, Decomposition-coarsening model of SiOC/HfO 2 ceramic nanocomposites upon isothermal anneal at 1300°C. J. Am. Ceram. Soc. **95**, 2290–2297 (2012). https://doi.org/10.1111/j.1551-2916.2012.05227.x
26. R. Anand, B.B. Nayak, S.K. Behera, Coarsening kinetics of nanostructured ZrO2 in Zr-doped SiCN ceramic hybrids. J. Alloys Compd. **811**, 151939 (2019). https://doi.org/10.1016/j.jallcom.2019.151939
27. A.J. Ardell, Trans-interface-diffusion-controlled coarsening of γ′ particles in Ni–Al alloys: commentaries and analyses of recent data. J. Mater. Sci. **55**, 14588–14610 (2020). https://doi.org/10.1007/s10853-020-05036-0
28. L. Lutterotti, M. Bortolotti, G. Ischia, I. Lonardelli, H.-R. Wenk, Rietveld texture analysis from diffraction images. Zeitschrift Für Krist. Suppl. **26**, 125–130 (2007). https://doi.org/10.1524/zksu.2007.2007.suppl_26.125
29. D. Watanabe, C. Watanabe, R. Monzen, Coarsening behavior of Co precipitates in Cu-Co alloys. Metall. Mater. Trans. A **39**, 725–732 (2008). https://doi.org/10.1007/s11661-008-9472-y
30. R. Monzen, K. Kita, Ostwald ripening of spherical Fe particles in Cu-Fe alloys. Philos. Mag. Lett. **82**, 373–382 (2002). https://doi.org/10.1080/09500830210137399
31. Z. Grzesik, G. Smoła, M. Stygar, J. Dąbrowa, M. Zajusz, K. Mroczka, M. Danielewski, Defect structure and transport properties in (Co, Cu, Mg, Ni, Zn)O high entropy oxide. J. Eur. Ceram. Soc. **39**, 4292–4298 (2019). https://doi.org/10.1016/j.jeurceramsoc.2019.06.018
32. B.J. Wuensch, T. Vasilos, Diffusion of transition metal ions in single-crystal MgO. J. Chem. Phys. **36**, 2917–2922 (1962). https://doi.org/10.1063/1.1732402
33. Z. Grzesik, M. Migdalska, Oxidation mechanism of Cu2O and defect structure of CuO at high temperatures. High Temp. Mater. Process. **30**, 277–287 (2011). https://doi.org/10.1515/htmp.2011.046
34. S.Z. Han, E.-A. Choi, S.H. Lim, S. Kim, J. Lee, Alloy design strategies to increase strength and its trade-offs together. Prog. Mater. Sci. **117**, 100720 (2021). https://doi.org/10.1016/j.pmatsci.2020.100720
35. H.A. Calderon, P.W. Voorhees, J.L. Murray, G. Kostorz, Ostwald ripening in concentrated alloys. Acta Metall. Mater. **42**, 991–1000 (1994). https://doi.org/10.1016/0956-7151(94)90293-3
36. D.A. Porter, K.E. Easterling, M.Y. Sherif, *Phase Transformations in Metals and Alloys*, 3rd edn. (CRC Press, Boca Raton, 2009)
37. R.P. Kolli, D.N. Seidman, Comparison of compositional and morphological atom-probe tomography analyses for a multicomponent Fe-Cu steel. Microsc. Microanal. **13**, 272–284 (2007). https://doi.org/10.1017/S1431927607070675
38. S.R. Summerfelt, C.B. Carter, Kinetics of NiFe2O4 Precipitation in NiO. J. Am. Ceram. Soc. **75**, 2244–2250 (1992). https://doi.org/10.1111/J.1151-2916.1992.TB04491.X
39. K.C. Yang, P. Shen, On the precipitation of coherent spinel nanoparticles in Ti-doped MgO. J. Solid State Chem. **178**, 661–670 (2005). https://doi.org/10.1016/j.jssc.2004.12.019
40. J. Hernández-Saz, M. Herrera, J. Pizarro, P.L. Galindo, M. Gonzalez, J. Abell, R.J. Walters, S.I. Molina, S. Duguay, Influence of the growth temperature on the composition distribution at sub-nm scale of InAlAsSb for solar cells. J. Alloys Compd. **763**, 1005–1011 (2018). https://doi.org/10.1016/j.jallcom.2018.05.333
41. A. Cerezo, S. Hirosawa, I. Rozdilsky, G.D.W. Smith, Combined atomic–scale modelling and experimental studies of nucleation

in the solid state. Philos. Trans. R. Soc. Lond. Ser. A **361**, 463–477 (2003). https://doi.org/10.1098/rsta.2002.1139

42. Z.W. Zhang, C.T. Liu, X.-L. Wang, K.C. Littrell, M.K. Miller, K. An, B.A. Chin, From embryos to precipitates: a study of nucleation and growth in a multicomponent ferritic steel. Phys. Rev. B. **84**, 174114 (2011). https://doi.org/10.1103/PhysRevB.84.174114
43. W.T. Donlon, T.E. Mitchell, A.H. Heuer, Precipitation in non-stoichiometric spinel. J. Mater. Sci. **17**, 1389–1397 (1982). https://doi.org/10.1007/BF00752251
44. T. Klein, M. Schachermayer, D. Holec, B. Rashkova, H. Clemens, S. Mayer, Impact of Mo on the ω o phase in β -solidifying TiAl alloys: an experimental and computational approach. Intermetallics **85**, 26–33 (2017). https://doi.org/10.1016/j.intermet.2017.01.011
45. S. Bai, P. Ying, Z. Liu, J. Wang, J. Li, Quantitative transmission electron microscopy and atom probe tomography study of Ag-dependent precipitation of Ω phase in Al-Cu-Mg alloys. Mater. Sci. Eng. A **687**, 8–16 (2017). https://doi.org/10.1016/j.msea.2017.01.045
46. T. Grygar, Z. Salatova, P. Vorm, Miscibility of CuO, NiO, and ZnO in their binary mixtures and its impact for reprocessing industrial wastes. Ceramics-Silikáty **45**, 121–127 (2001)
47. L.A. Zabdyr, O.B. Fabrichnaya, Phase equilibria in the cobalt oxide-copper oxide system. J. Phase Equilib. **23**, 149–155 (2002). https://doi.org/10.1361/1054971023604161
48. M. Paranthaman, K.A. David, T.B. Lindemer, Phase equilibria of the MgO-Cu2O-CuO system. Mater. Res. Bull. **32**, 165–173 (1997). https://doi.org/10.1016/S0025-5408(96)00184-5
49. A. Navrotsky, Thermodynamic relations among olivine, spinel, and phenacite structures in silicates and germanates. III. The system CuOMgOGeO2. J. Solid State Chem. **11**, 10–16 (1974). https://doi.org/10.1016/0022-4596(74)90140-6
50. D. Darbar, M.R. Anilkumar, V. Rajagopalan, I. Bhattacharya, H.I. Elim, T. Ramakrishnappa, F.I. Ezema, R. Jose, M.V. Reddy, Studies on spinel cobaltites, MCo2O4 (M = Mn, Zn, Fe, Ni and Co) and their functional properties. Ceram. Int. **44**, 4630–4639 (2018). https://doi.org/10.1016/j.ceramint.2017.12.010
51. A.J. Ardell, V. Ozolins, Trans-interface diffusion-controlled coarsening. Nat. Mater. **4**, 309–316 (2005). https://doi.org/10.1038/nmat1340
52. B.J. Wuensch, W.C. Steele, T. Vasilos, Cation self-diffusion in single-crystal MgO. J. Chem. Phys. **58**, 5258–5266 (1973). https://doi.org/10.1063/1.1679138
53. H. Nakajima, S. Yamaguchi, K. Iwasaki, H. Morita, H. Fujimori, Y. Fujino, Interdiffusion and interfacial reaction between an YBa 2 Cu 3 O x thin film and substrates. Appl. Phys. Lett. **53**, 1437–1439 (1988). https://doi.org/10.1063/1.100460
54. R. Freer, Self-diffusion and impurity diffusion in oxides. J. Mater. Sci. **15**, 803–824 (1980). https://doi.org/10.1007/BF00552089
55. A.S. Nowick, Defects in ceramic oxides. MRS Bull. **16**, 38–41 (1991). https://doi.org/10.1557/S0883769400055500
56. C.-M. Lin, V.S. Stubican, Influence of ionic charge on diffusion in the surface layer of magnesia. J. Am. Ceram. Soc. **70**, 73–74 (1987). https://doi.org/10.1111/j.1151-2916.1987.tb04989.x
57. D. Samal, H. Tan, Y. Takamura, W. Siemons, J. Verbeeck, G. Van Tendeloo, E. Arenholz, C.A. Jenkins, G. Rijnders, G. Koster, Direct structural and spectroscopic investigation of ultrathin films of tetragonal CuO: Six-fold coordinated copper. EPL **105**, 17003 (2014). https://doi.org/10.1209/0295-5075/105/17003
58. G. Peralta, D. Puggioni, A. Filippetti, V. Fiorentini, Jahn-Teller stabilization of magnetic and orbital ordering in rocksalt CuO. Phys. Rev. B. **80**, 140408 (2009). https://doi.org/10.1103/PhysRevB.80.140408
59. C.M. Rost, Z. Rak, D.W. Brenner, J.-P. Maria, Local structure of the Mg x Ni x Co x Cu x Zn x O(x =0.2) entropy-stabilized oxide: An EXAFS study. J. Am. Ceram. Soc. **100**, 2732–2738 (2017). https://doi.org/10.1111/jace.14756
60. X.-Q. Chen, C.L. Fu, C. Franchini, R. Podloucky, Hybrid density-functional calculation of the electronic and magnetic structures of tetragonal CuO. Phys. Rev. B. **80**, 094527 (2009). https://doi.org/10.1103/PhysRevB.80.094527
61. C.-Y. Pan, P. Shen, Spinel precipitation in Sn4+-doped Co1−xO polycrystals with dispersed Co2+xSn1−xO4 particles. Ceram. Int. **36**, 2137–2145 (2010). https://doi.org/10.1016/j.ceramint.2010.05.023
62. W. Wei, W. Chen, D.G. Ivey, Rock salt–spinel structural transformation in anodically electrodeposited Mn–Co–O nanocrystals. Chem. Mater. **20**, 1941–1947 (2008). https://doi.org/10.1021/cm703464p
63. K.C. Yang, P. Shen, D. Gan, Defect microstructures of TiO2 rutile due to Zr4+ dissolution and expulsion. J. Solid State Chem. **179**, 3478–3483 (2006). https://doi.org/10.1016/j.jssc.2006.07.020
64. J.-O. Andersson, T. Helander, L. Höglund, P. Shi, B. Sundman, Thermo-Calc & DICTRA, computational tools for materials science. Calphad **26**, 273–312 (2002). https://doi.org/10.1016/S0364-5916(02)00037-8